

A Highly Emissive Surface Layer in Mixed-Halide Multication Perovskites

Andaji-Garmaroudi, Zahra; Abdi-Jalebi, Mojtaba; Guo, Dengyang; Macpherson, Stuart; Sadhanala, Aditya; Tennyson, Elizabeth M.; Ruggeri, Edoardo; Anaya, Miguel; Savenije, Tom J.; More Authors

DOI

[10.1002/adma.201902374](https://doi.org/10.1002/adma.201902374)

Publication date

2019

Document Version

Final published version

Published in

Advanced Materials

Citation (APA)

Andaji-Garmaroudi, Z., Abdi-Jalebi, M., Guo, D., Macpherson, S., Sadhanala, A., Tennyson, E. M., Ruggeri, E., Anaya, M., Savenije, T. J., & More Authors (2019). A Highly Emissive Surface Layer in Mixed-Halide Multication Perovskites. *Advanced Materials*, 31(42), Article 1902374. <https://doi.org/10.1002/adma.201902374>

Important note

To cite this publication, please use the final published version (if applicable). Please check the document version above.

Copyright

Other than for strictly personal use, it is not permitted to download, forward or distribute the text or part of it, without the consent of the author(s) and/or copyright holder(s), unless the work is under an open content license such as Creative Commons.

Takedown policy

Please contact us and provide details if you believe this document breaches copyrights. We will remove access to the work immediately and investigate your claim.

A Highly Emissive Surface Layer in Mixed-Halide Multication Perovskites

Zahra Andaji-Garmaroudi, Mojtaba Abdi-Jalebi, Dengyang Guo, Stuart Macpherson, Aditya Sadhanala, Elizabeth M. Tennyson, Edoardo Ruggeri, Miguel Anaya, Krzysztof Galkowski, Ravichandran Shivanna, Kilian Lohmann, Kyle Frohna, Sebastian Mackowski, Tom J. Savenije, Richard H. Friend, and Samuel D. Stranks*

Mixed-halide lead perovskites have attracted significant attention in the field of photovoltaics and other optoelectronic applications due to their promising bandgap tunability and device performance. Here, the changes in photoluminescence and photoconductance of solution-processed triple-cation mixed-halide ($\text{Cs}_{0.06}\text{MA}_{0.15}\text{FA}_{0.79}\text{Pb}(\text{Br}_{0.4}\text{I}_{0.6})_3$) perovskite films (MA: methylammonium, FA: formamidinium) are studied under solar-equivalent illumination. It is found that the illumination leads to localized surface sites of iodide-rich perovskite intermixed with passivating PbI_2 material. Time- and spectrally resolved photoluminescence measurements reveal that photoexcited charges efficiently transfer to the passivated iodide-rich perovskite surface layer, leading to high local carrier densities on these sites. The carriers on this surface layer therefore recombine with a high radiative efficiency, with the photoluminescence quantum efficiency of the film under solar excitation densities increasing from 3% to over 45%. At higher excitation densities, nonradiative Auger recombination starts to dominate due to the extremely high concentration of charges on the surface layer. This work reveals new insight into phase segregation of mixed-halide mixed-cation perovskites, as well as routes to highly luminescent films by controlling charge density and transfer in novel device structures.

(LEDs).^[1–5] These perovskites, which are typically deposited as a thin film from solutions of organic cation and metal halide salts, exhibit promising optoelectronic properties including long charge-carrier diffusion lengths, strong absorption coefficients, and potentially low fabrication costs.^[6–8] However, perovskite thin films such as MAPbI_3 (MA: methylammonium) typically show low external luminescence quantum efficiencies (<5%) under PV or LED device operation conditions, meaning they are still far from achieving their efficiency limits.^[9] These low luminescence yields are attributed to a moderate defect density leading to nonradiative decay pathways, though these can at least in part be mitigated by carrier filling at higher excitation densities,^[10] light-induced trap annihilation,^[11–13] or passivation treatments.^[14–16]

One of the most exciting aspects of these materials is the ability to continually tune the bandgap and lattice parameter by mixing different fractions of halides into

Metal-halide perovskites have emerged as attractive materials for a variety of high-performance optoelectronic applications including solar photovoltaics (PV) and light-emitting diodes

the structure.^[17–19] For example, the $\text{MAPb}(\text{Br}_x\text{I}_{1-x})_3$ ($0 \leq x \leq 1$) perovskite family exhibits excellent bandgap tunability over the range 1.6–2.3 eV ($x = 0–1$, respectively), which, in principle,

Z. Andaji-Garmaroudi, Dr. M. Abdi-Jalebi, S. Macpherson, Dr. A. Sadhanala, Dr. E. M. Tennyson, E. Ruggeri, Dr. M. Anaya, Dr. K. Galkowski, Dr. R. Shivanna, K. Lohmann, K. Frohna, Prof. R. H. Friend, Dr. S. D. Stranks
Cavendish Laboratory
JJ Thomson Avenue
Cambridge CB3 0HE, UK
E-mail: sds65@cam.ac.uk

 The ORCID identification number(s) for the author(s) of this article can be found under <https://doi.org/10.1002/adma.201902374>.

© 2019 The Authors. Published by WILEY-VCH Verlag GmbH & Co. KGaA, Weinheim. This is an open access article under the terms of the Creative Commons Attribution License, which permits use, distribution and reproduction in any medium, provided the original work is properly cited.

The copyright line for this article was changed on 9 September 2019 after original online publication.

DOI: 10.1002/adma.201902374

D. Y. Guo, Prof. T. J. Savenije
Department of Chemical Engineering
Delft University of Technology
van der Maasweg 9 2629 HZ, Delft, The Netherlands

Dr. A. Sadhanala
Clarendon Laboratory
Department of Physics
University of Oxford
Parks Road, Oxford OX1 3PU, UK

Dr. K. Galkowski, Prof. S. Mackowski
Institute of Physics
Faculty of Physics
Astronomy and Informatics
Nicolaus Copernicus University
5th Grudziądzka St. 87-100, Toruń, Poland

opens up new applications in building-integrated PV, large-bandgap absorbers in tandem PV configurations,^[20] colored lasers, and LEDs.^[3] Nevertheless, these mixed-halide perovskites show even lower luminescence quantum efficiencies than their single halide counterparts.^[21] Moreover, when such perovskite compositions containing more than $\approx 20\%$ bromide are incorporated in solar cells, they show a decrease in open-circuit voltage over time under illumination despite the increased bandgap.^[17,22] Hoke et al. first showed that the decreased voltage observations were related to the formation of low-energy iodide-rich domains under illumination.^[23] This suggestion was based on observations of the photoluminescence (PL) spectra shifting to longer wavelengths on a time scale of seconds under solar-equivalent illumination conditions due to a light-induced bromide–iodide segregation, with the charge carriers funneling to and recombining on the lower-energy iodide-rich sites.^[24,25] The mechanism of the photoinduced ionic segregation is currently a topic under debate, though consensus suggests that the process involves halide defects (vacancies and/or interstitials) driven by a gradient in carrier generation through the film thickness.^[12,24,26–29] “Triple-cation” perovskites, in which a mixture of MA, formamidinium (FA), and cesium (Cs) is used as the monovalent A-site cations, have recently attracted significant attention due to their high efficiency and stability in solar cells.^[30] It has been proposed that such mixed-cation compositions could impede the ionic segregation processes,^[31] thereby further impacting carrier recombination. Nevertheless, in each of these systems, the chemical and structural nature of the segregated regions, and the local charge-carrier recombination properties of the resulting film, have not yet been determined.

Here, we study the changes in the optical bandgap and the micro- and macroscale PL properties of mixed-cation lead mixed-halide ($\text{Cs}_{0.06}\text{MA}_{0.15}\text{FA}_{0.79}\text{Pb}(\text{Br}_{0.4}\text{I}_{0.6})_3$) perovskite films under equivalent solar illumination conditions. We find that illumination under ambient laboratory conditions leads to the formation of spatially inhomogeneous iodide-rich perovskite seeds on the surface of the perovskite film that grow in size over time. We show that photogenerated charge carriers transfer onto these domains and recombine with high radiative efficiency, with external PL quantum efficiencies of the film reaching over 45% at solar illumination intensities. This high radiative efficiency is due to a combination of a photoinduced trap reduction and a high local concentration of charges on the low-bandgap (LG) emitting sites ensuring radiative bimolecular processes dominate recombination. We propose a mechanism in which a highly emissive surface layer of passivated iodide-rich perovskite is formed during illumination which acts as a radiative recombination sink for charge carriers. We show that there is a fine balance between the radiative recombination and nonradiative (Auger) processes, with the latter dominating at higher excitation fluences when the charge-carrier density on the surface layer becomes extremely high. This work demonstrates new insight into the impact of photoinduced phase segregation in mixed-cation lead mixed-halide perovskites, leading the way toward highly emissive films and novel energy-harvesting or -emitting device structures that could exploit controlled energy transfer.

Thin films of the triple-cation mixed-halide ($\text{Cs}_{0.06}\text{MA}_{0.15}\text{FA}_{0.79}\text{Pb}(\text{Br}_{0.4}\text{I}_{0.6})_3$) perovskite with a thickness of ≈ 550 nm (unless stated otherwise) were spin-coated on glass

substrates from precursor solutions comprised of the relevant salts dissolved in *N,N*-dimethylformamide (DMF) and dimethyl sulfoxide (DMSO) (see the “Experimental Section” for further details and Figure S1 in the Supporting Information for scanning electron microscope (SEM) images of the films). We note that all subsequent measurements were performed under ambient laboratory conditions in this work including air and humidity, unless stated otherwise.

We performed photothermal deflection spectroscopy (PDS) measurements to investigate the optical absorption of the films. PDS is an ultrasensitive absorption measurement technique, which allows detection and quantification of sub-bandgap features provided the films are sufficiently thin (in this case 200 nm) to avoid saturation of the above-bandgap absorption.^[32–36] Figure 1a shows the PDS spectra for a sample before (black circles) and after (red squares) light treatment for 30 min with a white-light LED source with an intensity approximately equivalent to 1 sun (see schematic in the inset showing the treatment). We observe the emergence of a redshifted band edge after light treatment. We interpret this as formation of another domain with a lower energy bandgap, which is in agreement with previous reports for $\text{MAPb}(\text{Br}_x\text{I}_{1-x})_3$.^[23,26] The absorbance level of the redshifted band edge for the treated film (≈ 790 nm) is $\approx 4\%$ of the absorbance at the higher-energy band edge (≈ 705 nm), indicating that the lower-bandgap component comprises $\approx 4\%$ of the total material (see Figure S2 in the Supporting Information for further discussion). A further analysis of the relative change in phase of the PDS signal suggests that this low-bandgap component may lie primarily on the surface of the film (see Figure S2 and further discussion in the Supporting Information). In addition, we find that the subgap absorption baseline (>830 nm) decreases after light treatment, suggesting that the surface trap state density is reduced in these mixed-halide perovskites after illumination. We propose that this light-induced trap annihilation is akin to that observed in the pure-iodide MA-based systems, in which light and atmospheric molecules can passivate surface traps.^[11–13,37] Therefore, the light treatment causes two effects in these mixed-halide perovskites: low-bandgap energy domains are formed (likely on the surface) along with the removal of a substantial density of subgap trap states.

To further assess the optical properties, we light-soaked a film with 1 sun equivalent laser excitation and recorded the PL spectra over a time period of 30 min (Figure 1b). The original high-energy peak (wide-bandgap, WG) initially rises in intensity over the first minutes, which we attribute to the reduction in trap state density under illumination as described above. After ≈ 1 min under these conditions, we see the emergence of a low-bandgap (LG) PL peak due to halide segregation and subsequent charge transfer to iodide-rich sites, as observed in previous works for $\text{MAPb}(\text{Br}_x\text{I}_{1-x})_3$.^[24] We find that this LG peak then rises substantially under continuous illumination and shifts toward longer wavelengths. After 30 min of light treatment, the LG peak dominates the emission. We observe similar effects when we sandwich the perovskite film between charge-injecting contacts typically used for LEDs (Figure S3, Supporting Information). We note that the time scales to reach steady-state (equilibrium) emission under solar-equivalent conditions for these mixed-cation, mixed-halide samples is ≈ 30 min. The equivalent photon dose for reaching this equilibrium is 18×10^4 mJ cm⁻²,

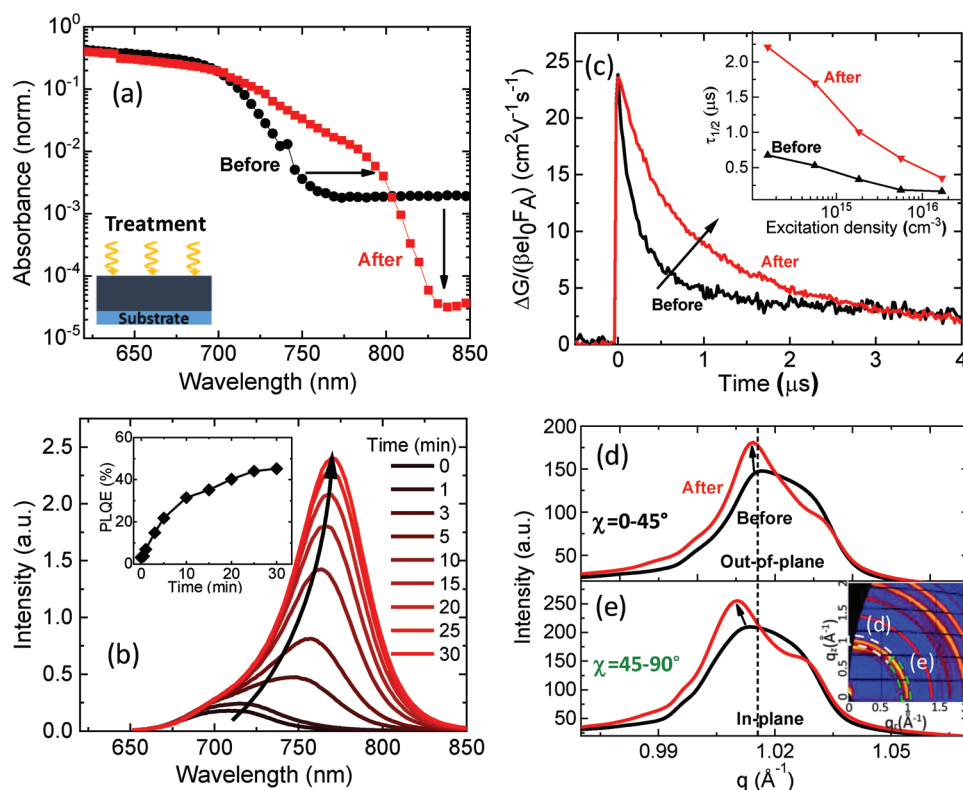


Figure 1. a) PDS spectra for $(\text{Cs}_{0.06}\text{MA}_{0.15}\text{FA}_{0.79})\text{Pb}(\text{Br}_{0.4}\text{I}_{0.6})_3$ perovskite films before (black circles) and after (red squares) 30 min of light treatment with a white-light LED source ($\approx 100 \text{ mW cm}^{-2}$). The spectra are normalized to the values at a wavelength of 387 nm. b) PL spectra of a $(\text{Cs}_{0.06}\text{MA}_{0.15}\text{FA}_{0.79})\text{Pb}(\text{Br}_{0.4}\text{I}_{0.6})_3$ perovskite film over time in ambient conditions under laser illumination (532 nm laser, $\approx 60 \text{ mW cm}^{-2}$) producing the equivalent number of excitations to 1 sun intensity. The inset shows the corresponding photoluminescence quantum efficiency (PLQE) over time under the same conditions. c) Photoconductance (TRMC) measurements performed on a film, with an excitation wavelength of 500 nm and an excitation density of $5.6 \times 10^{15} \text{ cm}^{-3}$, before (black) and after (red) light treatment for 30 min under white-light 1 sun equivalent illumination. Inset: Half lifetimes versus excitation density extracted from TRMC transients before and after light treatment (Figure S5, Supporting Information). d) Out-of-plane ($0^\circ < \chi < 45^\circ$) and e) in-plane ($45^\circ < \chi < 90^\circ$) azimuthally integrated line profiles (χ indicates the azimuthal angle from the q_z -axis) taken from GIWAXS profiles corresponding to the perovskite ($q \approx 1 \text{ \AA}^{-1}$) peak before and after the light treatment with a 532 nm laser at an intensity equivalent to 0.3 suns (see Figure S7 in the Supporting Information for additional time points under illumination). The corresponding integrated regions are shown in the 2D GIWAXS diffraction pattern from the perovskite film (at $t = 0.0 \text{ h}$) in the inset.

which is three orders of magnitude higher than the photon dose required for the single cation $\text{MAPb}(\text{Br}_x\text{I}_{1-x})_3$ counterparts ($\approx 675 \text{ mJ cm}^{-2}$),^[23] suggesting that the ionic segregation processes and light-induced passivation effects are slowed in these mixed-cation compositions. We also note that the specific light dose required to approach a stabilized emission intensity is sensitive to the local environmental conditions such as humidity level^[27,38] and, thus, for all subsequent measurements presented herein, we simultaneously perform in situ PL measurements to monitor the extent of the light-treatment effects. We also find that the segregation processes are partially reversible with storage in the dark, reaching steady-state values of PL intensity and peak wavelength after $\approx 90 \text{ min}$ though the films still remain more emissive (a factor of 2) and the PL peak is still slightly redshifted with respect to the untreated film (Figure S4, Supporting Information).

In Figure 1b, inset, we show the growth of external PL quantum efficiency (PLQE) with time under laser illumination equivalent to 1 sun. We observe a substantial increase in PLQE under illumination from 3% to 45% following the light treatment. We note that further optical modeling would be required

to determine an internal luminescence quantum yield after accounting for light outcoupling, though given the extremely thin nature of the surface layer we do not expect that changes in light outcoupling alone can explain such a substantial increase in luminescence. These PL results show that photoexcited carriers in these mixed-cation mixed-halide perovskites funnel toward the LG iodide-rich domains, on which they recombine with remarkably high radiative efficiency.

In order to understand how the light treatment impacts charge transport behavior, we performed time-resolved microwave conductivity (TRMC) measurements. TRMC is a pump-probe technique that monitors the change in photoconductance (ΔG) after a short laser excitation pulse, allowing the investigation of mobile charge-carrier dynamics.^[39] In Figure 1c, we show ΔG of the perovskite films excited with a 500 nm pulsed laser, before and after light treatment for 30 min under 1 sun illumination in ambient conditions. The similar signal heights in both cases ($\approx 24 \text{ cm}^2 \text{ V}^{-1} \text{ s}^{-1}$) suggest that the bulk mobility properties are largely unaffected by the treatment. However, we find that the lifetime of charge carriers rises substantially after light treatment in ambient conditions, as we reported

previously for MAPbI₃.^[37] This increase in lifetime is likely due to the lower trap densities in the treated compositions; we note that we do not expect significant contributions to the TRMC signal from the surface sites due to the small size of these domains (see the following) restricting their effective mobility. The inset in Figure 1c shows that the corresponding half-lifetimes ($\tau_{1/2}$) are consistently longer for the treated sample than before treatment for each excitation density, with the lifetime at the lowest fluence ($0.6 \times 10^{15} \text{ cm}^{-2}$) increasing by over a factor of 3 from 0.68 to 2.2 μs (see Figure S5 for decays at different fluences and Figure S6 for different excitation wavelengths in the Supporting Information). These TRMC results suggest that the highly emissive surface layer does not compromise bulk charge-carrier mobility, but that the resulting carriers remain mobile for long lifetimes.

To monitor changes in the surface structural properties of the film during the light treatment, we performed grazing-incidence wide-angle X-ray scattering (GIWAXS) measurements over time under light illumination with ≈ 0.3 sun equivalent intensity; simultaneous *in situ* PL measurement confirmed we observed the same effects as Figure 1b albeit over longer time periods due to the lower excitation intensity (see Figure S7 in the Supporting Information and “Experimental Section” for further details). Figure 1d,e shows the respective out-of-plane ($0^\circ < \chi < 45^\circ$) and in-plane ($45^\circ < \chi < 90^\circ$) azimuthally integrated line profiles taken from the 2D GIWAXS diffractograms corresponding to the perovskite peak at $q \approx 1 \text{ \AA}^{-1}$ (based on cubic unit cell;^[40] see the inset denoting the integrated regions from the 2D diffractogram at $t = 0 \text{ h}$ and Figure S8 in the Supporting Information for the diffractograms at later time snapshots). During the light treatment, we observe peak splitting and growth of the lower q peak especially in the in-plane orientation ($45^\circ < \chi < 90^\circ$; Figure 1e). The rise of the lower- q peak is due to the emergence of a perovskite phase on the surface with larger lattice parameter, which we interpret to be a phase with higher iodide content than the surrounding mixed-halide phase (higher- q peak).^[41] This rise in iodide-rich low- q perovskite peak while the higher- q mixed-iodide/bromide perovskite peak remains approximately constant is consistent with iodide preferentially migrating to the surface to form these domains. The dominance of this iodide-rich surface peak after the illumination is consistent with our spectroscopic PDS and PL results, which suggested that an LG iodide-rich perovskite surface layer forms. The fact that the overall peak shift toward lower q -values is most pronounced in the in-plane integrated line profiles (Figure 1e) indicates that the iodide-rich domains preferentially orient in the vertical direction with respect to the film surface. Over time under illumination, we also observe a peak splitting of the PbI₂ peak ($q \approx 0.9 \text{ \AA}^{-1}$),^[42,43] which we speculate to be related to the interaction with moisture and/or a strained environment on the surface, potentially influenced by the surface environment becoming more iodide-rich (see Figure S7 in the Supporting Information).

We also performed the same simultaneous PL and GIWAXS measurements under inert dry helium (Figure S9, Supporting Information). We note that the experimental geometry only allows flow of the helium gas over the sample, so we cannot exclude the presence of low levels of oxygen and humidity. We find that the rise of the low-bandgap PL peak, the luminescence

increase, and the splitting of the perovskite and PbI₂ diffraction peaks after the same illumination time are not nearly as significant as in the ambient atmosphere case. These results suggest that the effects are significantly slowed down with reduced levels of oxygen and humidity. We propose that this is a combination of moisture and/or oxygen speeding up ionic segregation and a passivation effect from moisture and/or oxygen.^[27,37,44–46]

These results collectively suggest that the light treatment leads to formation of a surface layer of well-passivated, iodide-rich LG perovskite crystallites. Subsequent PL measurements from the front- and back sides of the sample show that the front-side treatment is not significantly affecting the non-illuminated rear side except at much thinner film thickness (Figure S10, Supporting Information). These results suggest that the photoinduced LG regions are located primarily on the illuminated surface and the emission from these sites is limited by carriers diffusing to them. As the iodide-rich sites form only $\approx 4\%$ of the treated film (cf., PDS in Figure 1a), we propose that the LG region is an extremely thin surface layer on the order of less than 10 nm.

To visualize these processes, we implement local photoluminescence imaging and monitor the changes of the perovskite film over time during light treatment. Figure 2a–h shows a time series of hyperspectral photoluminescence maps measured *in situ* with the region of interest under continuous white-light illumination equivalent to ≈ 3 suns, with the top (bottom) row showing the intensity of the WG (LG) peaks (see Figure S11 in the Supporting Information for the spatially integrated PL spectra). We see that the emission from the WG regions is initially dominant and spatially heterogeneous, while we do not observe significant LG emission before the treatment ($t = 0 \text{ min}$; Figure 2a,e). During the light treatment, we observe the emergence of localized LG “seeds,” corresponding to iodide-rich domains (Figure 2f). The number and intensity of these seeds continue to grow over time while the film is subjected to continuous illumination (Figure 2g). This result suggests that the halide segregation occurs heterogeneously on the surface. The emission from the WG regions during the light treatment (Figure 2b,c) also increases in intensity, consistent with our macroscopic observations (cf. Figure 1b). We then continue to illuminate the sample until the PL reaches a stabilized level. We observe that the intensity and spatial coverage of the LG emission regions grow substantially and eventually dominate the PL distribution (Figure 2h), while the WG emission only slightly increases in intensity and displays a more homogeneous distribution (Figure 2d). We note that we could not detect any PbI₂ emission from the film before or after the treatment, likely due to the low PL efficiency of PbI₂.

In Figure 2i, we overlay the PL map of the WG peak at $t = 0 \text{ min}$ (Figure 2a) and the PL map of the LG peak at $t = 180 \text{ min}$ (Figure 2h). This shows that the initial PL distribution impacts the location of the subsequent LG regions; the regions that are brighter in LG emission after the treatment (red regions) are primarily located in the areas that are initially dark at $t = 0 \text{ min}$. Since low-emission-intensity (dark) areas correspond to higher trap state densities,^[47] this result reveals a relationship between phase segregation and charge-carrier traps.^[26,27,48] In Figure 2j, we show the distributions of the

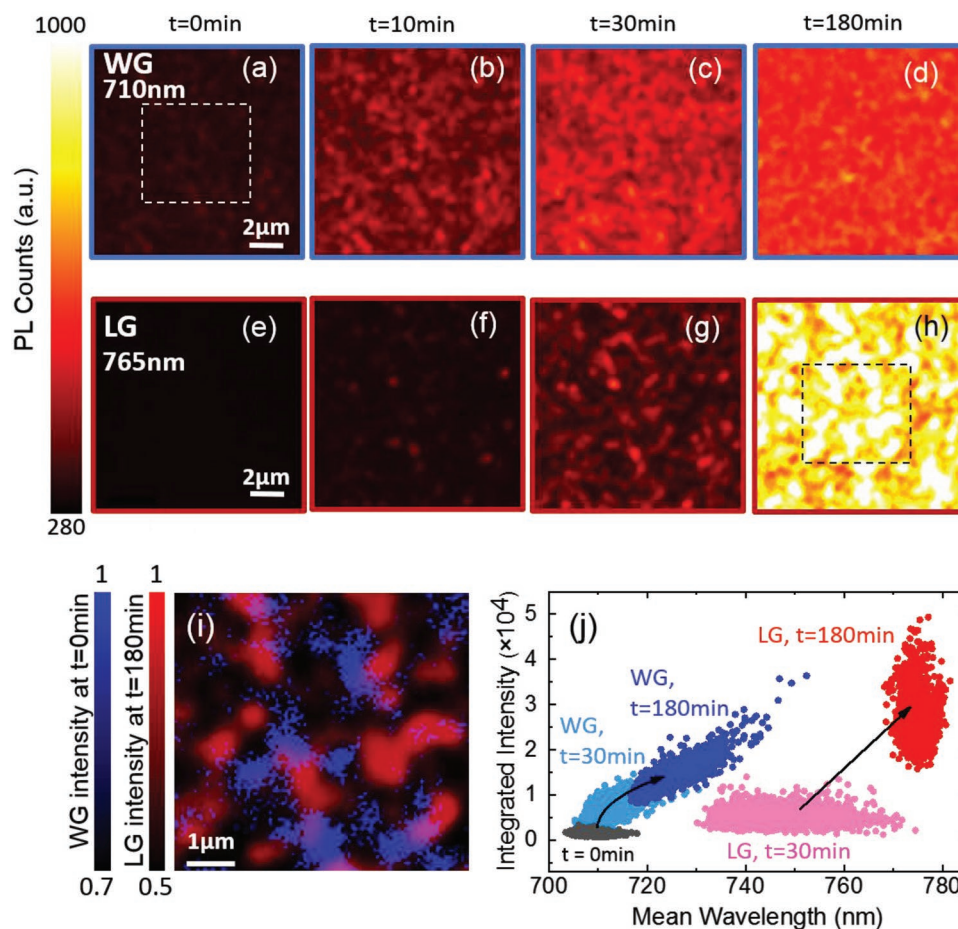


Figure 2. a–h) In situ hyperspectral photoluminescence maps on the same region for WG peaks (a–d) and LG peaks (e–h) in $(\text{Cs}_{0.06}\text{MA}_{0.15}\text{FA}_{0.79})\text{Pb}(\text{Br}_{0.4}\text{I}_{0.6})_3$ perovskite thin films over time under white-light illumination with an intensity of 290 mW cm^{-2} (equivalent to ≈ 3 suns) for the sample before treatment ($t = 0$), during the treatment (10 and 30 min), and once the emission intensity reaches stabilized emission (180 min). Maps were taken with 405 nm laser excitation with ≈ 1 sun intensity (50 mW cm^{-2}) and all measurements were performed in an ambient atmosphere. i) Overlays of the PL maps of the WG peak at $t = 0$ min and PL map of the LG peak at $t = 180$ min from the zoomed-in area denoted by the dashed boxes in (a) and (h), respectively. PL intensities are normalized to their maximum values. j) Distributions of the integrated intensity of the WG and LG peaks versus their emission wavelength in the PL maps extracted from the spectra (see the Supporting Information for details).

intensity of WG and LG peaks versus their mean wavelength for all pixels in the PL maps. We observe that the emission wavelength distribution broadens for both LG and WG peaks during the light-treatment process ($t = 30$ min) before narrowing as the emission approaches stabilized values, particularly for the LG distribution. This suggests that during the light-induced ion segregation processes, there is a distribution of intermediate emitting compositions that are spatially distributed but, once the phase segregation is complete (corresponding to stabilized emission properties), the luminescence predominantly originates from the low-bandgap iodide-rich (radiative) recombination domains. This is again consistent with an efficient energy transfer from the WG to LG sites on which charges predominantly recombine radiatively. We note that the final LG intensity distribution remains quite broad, indicating that the surface layer luminescence intensity remains spatially heterogeneous.

To further probe the emission mechanism of the treated films after light treatment, we measured transient PL spectra of these films. We treated the sample using a continuous-wave (CW) laser source equivalent to 1 sun (532 nm , $\approx 60 \text{ mW cm}^{-2}$),

and at various stages under the illumination we collected transient PL spectra using a 550 nm pulsed excitation laser. We also simultaneously collected steady-state PL during the light treatment to monitor progress of the treatment (Figure S12, Supporting Information). We show in Figure 3 the normalized transient PL spectra over time after pulsed excitation at two different fluences (the lower fluence is equivalent to 1 sun) for the film before the treatment, after 45 min of treatment when it is partially treated in this experiment (based on the steady-state PL; Figure S12, Supporting Information), and after 90 min when the emission from the film reaches stabilized levels (completely treated). The transient PL spectra are normalized to the maximum intensity of the WG peak in order to monitor the relative fraction of LG and WG emission over time after illumination (see Figure S13 for other intermediate fluences and Figure S14 for PL decays in the Supporting Information). The maximum peak intensities for the WG and LG energies just after pulse excitation (at $t = 4$ ns) as a function of charge excitation density are also shown in Figure 3c,f,i (see the Supporting Information for details). We find that the emission is dominated by the WG

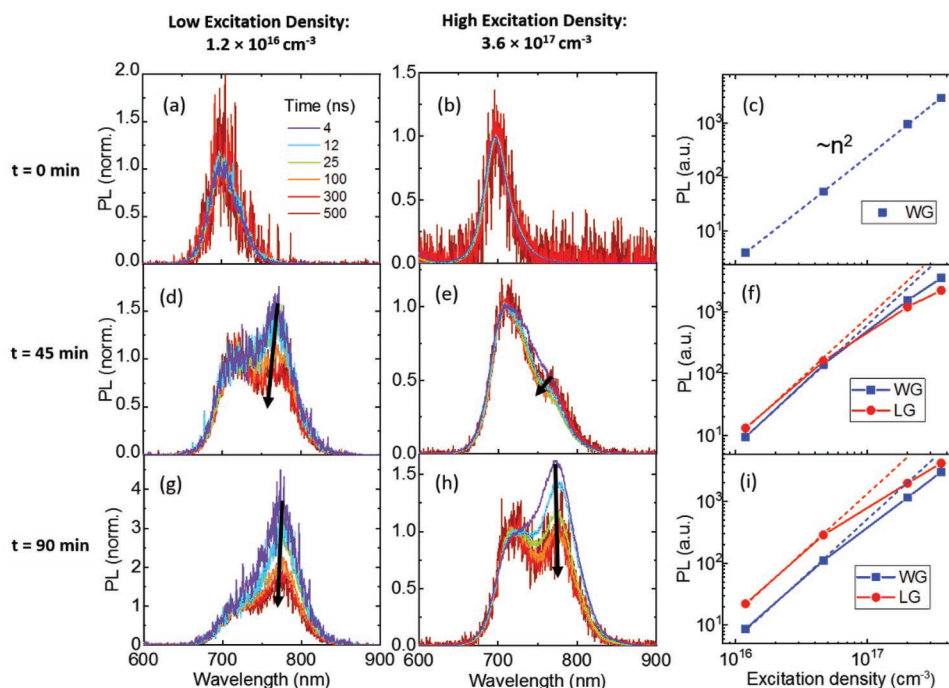


Figure 3. Transient photoluminescence spectra from $(\text{Cs}_{0.06}\text{MA}_{0.15}\text{FA}_{0.79})\text{Pb}(\text{Br}_{0.4}\text{I}_{0.6})_3$ films normalized at the WG peak. The sample is probed following light treatment under laser illumination (CW 532 nm laser, $\approx 60 \text{ mW cm}^{-2}$) excited with a wavelength of 550 nm for two different pulse fluences of $1.2 \times 10^{16} \text{ cm}^{-3}$ (equivalent to 1 sun) and $3.6 \times 10^{17} \text{ cm}^{-3}$ for the film before the treatment (a,b), after 45 min of treatment (partially treated) (d,e), and after 90 min of treatment (fully treated) (g,h). c,f,i) The initial peak intensity corresponding to WG and LG energies just after pulse excitation (which were extracted from fits to the spectra with Gaussian functions) as a function of charge excitation density. Dashed lines in (c) denote a second-order recombination rate; in (f) and (i), these bimolecular lines are shifted appropriately as a guide to the eye to the appropriate data set.

peak before light treatment for both the low ($1.2 \times 10^{16} \text{ cm}^{-3}$; Figure 3a) and high ($3.6 \times 10^{17} \text{ cm}^{-3}$; Figure 3b) excitation densities, and there is negligible change in the PL spectra at different time snapshots. The maximum intensity of the PL peak versus charge excitation for the film before treatment (Figure 3c) shows that the initial PL intensity scales quadratically with the carrier excitation density; the dashed lines in Figure 3c denote a second-order rate relationship in which initial PL goes as the square of excitation density.^[49] This scaling is the signature of bimolecular recombination and is consistent with radiative recombination expected from a bulk film across this fluence range.^[50]

The $t = 4 \text{ ns}$ snapshots in the partially treated sample (Figure 3d) reveal that the LG peak from the film surface dominates at low excitation density, while the bulk WG peak is more dominant at high fluence (Figure 3e). The plot of the maximum intensity of the LG and WG peaks, extracted from Gaussian fits to the spectra, versus charge excitation for the partially treated film (Figure 3f) shows a clear deviation from bimolecular behavior (the dashed line) in the LG peak at higher excitation densities. The WG peak also deviates, but to a lesser extent. We propose that the deviation of the LG peak from a bimolecular dependence is due to an increased contribution of Auger recombination at the higher carrier densities. The Auger recombination contribution is cubic in carrier density, and therefore starts to dominate over the radiative rate at high excitation densities.^[49,51] As the LG regions are very small and localized in partially treated samples (cf. Figure 2h,i), the effective local carrier density due to carriers funneling onto these sites will be extremely high. In fact, given that the onset of Auger recombination occurs in the

partially treated sample at $\approx 4 \times 10^{16} \text{ cm}^{-3}$ (Figure 3f) whereas we do not observe any Auger behavior even up to $\approx 4 \times 10^{17} \text{ cm}^{-3}$ in the untreated sample (Figure 3c), the carrier density is at least one order of magnitude higher in the LG sites compared to that in the untreated film. Such a high concentration of charges on LG sites increases the nonradiative (Auger) to radiative (bimolecular) recombination ratio in these surface regions compared to bulk WG regions, which explains the decrease in fraction of the LG peak relative to the WG peak in these partially treated films at high excitation density (Figure 3e). We propose that the deviation of the WG peak from a bimolecular dependence is due to increasing competitiveness of energy transfer from WG to LG regions for the treated samples. Furthermore, the LG peak fraction in Figure 3d,e decreases after the initial pulse as time proceeds at both excitation densities. We propose that the faster overall recombination on the LG sites is due to the higher charge densities on the thin LG surface layer than in the bulk WG film.

We see in Figure 3g that the LG peak dominates the emission at low excitation density in the fully treated sample. We note that the results for low excitation density are consistent with our macro-PL measurements performed at similar fluence (Figure 1b). At higher excitation density (Figure 3h), the initial $t = 4 \text{ ns}$ PL snapshot is also dominated by the LG emission though the relative fraction of the WG peak is higher than in the lower excitation density case. The PL signal of the LG peak plotted over the charge-carrier density for the fully treated sample also shows deviation from a bimolecular dependence (Figure 3i). Since the LG domains grow in size as the light treatment continues toward completion (cf. Figure 2h), we expect less Auger

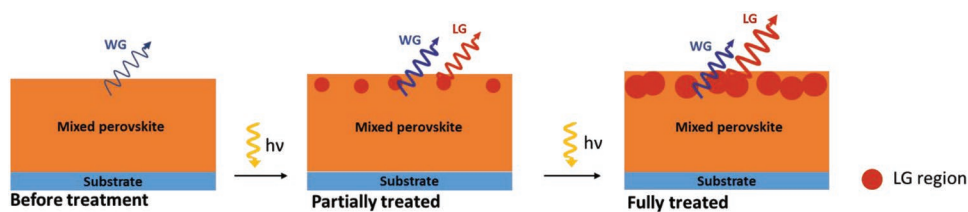


Figure 4. Cross-sectional schematic of a mixed-halide film under various stages of light treatment showing photoinduced LG regions located close to the illuminated surface, with the WG emission from the bulk mixed perovskite.

recombination in the fully treated film as carriers are in fact less concentrated compared to the partially treated sample. Nevertheless, Auger recombination does still reduce the fraction of LG (compared to WG) at higher fluence, which is indicative of significant carrier accumulation in the LG-rich surface. Again, we suggest that the slight deviation of the WG from the bimolecular dependence is due to fast energy transfer from the WG to LG regions at high excitation fluence. In addition, we again observe a decrease in the LG peak fraction after the initial pulse as time proceeds in the fully treated film (Figure 3g,h), which is due to enhanced effective charge densities within the LG regions.

We summarize our proposed mechanism for the changes in material and charge dynamics during light treatment in the schematic in **Figure 4**. From the PDS results, we found that there is initially a sizeable density of subgap states through the bandgap of the mixed-halide perovskites. After light treatment, the density of trap states is reduced, concomitant with the formation of LG energy domains. The LG regions are located close to the illuminated surface of the film and within the first ≈ 10 nm of the surface. Our GIWAXS measurements are consistent with this surface layer being iodide rich, with these domains showing a preferred vertical orientation with respect to the film surface. Through spatially resolved PL imaging, we found that the initial size of the LG regions is small and localized. Furthermore, charges efficiently funnel to LG sites, making the effective photoinduced carrier density on these sites extremely high; thus, nonradiative Auger recombination dominates under relatively high excitation densities. As we increase the light treatment time toward a steady-state emission output, the iodide-rich domains grow in size and detectable number, and the fraction of radiative recombination starts to dominate over Auger processes. This leads to a highly emissive iodide-rich surface layer, with the PLQE exceeding 45% under solar illumination conditions.

In summary, we studied the changes in the micro- and macro-scale optical properties of $(\text{Cs}_{0.06}\text{MA}_{0.15}\text{FA}_{0.79})\text{Pb}(\text{Br}_{0.4}\text{I}_{0.6})_3$ perovskite films under solar equivalent illumination conditions. Following light treatment of these films, we observe the formation of an emissive and low-bandgap (LG) passivated iodide-rich surface layer on the light-treated surface. This results in efficient charge transfer from bulk wide-bandgap (WG) to the surface LG sites, leading to high effective carrier densities on the LG sites. We find that the fraction of radiative and nonradiative (Auger) emission depends sensitively on the extent of formation of the surface layer and carrier fluence, allowing a new lever to control carrier recombination behavior. We demonstrate that under solar illumination fluences we can achieve PL quantum efficiencies of $\approx 45\%$.

This work sheds new light on the halide segregation processes in alloyed perovskites, including a route to highly emissive films. These energy-transfer processes open up opportunities to use local stoichiometry to better control the energy cascade and for designing novel, highly emissive devices around this concept. For instance, by light-soaking these systems in this way, we create a self-assembled color conversion heterostructure device in which incident high-energy photons generate carriers that funnel to the surface layer on which they recombine radiatively emitting lower-energy photons. In this structure, we can achieve efficient bimolecular recombination behavior even at extremely low excitation densities, i.e., 1 sun equivalent or even substantially lower, due to the high concentration of charges on LG sites. This leads to strong radiative emission even at low excitation densities, which will be important for applications including sensitive light harvesters, photodetectors, and lasing.

Experimental Section

Materials: Lead compounds were purchased from TCI; the organic cations were purchased from Dyesol; cesium iodide was obtained from Alfa Aesar; colloidal zinc oxide nanoparticles doped with aluminum oxide (AZO) were purchased from Nanograde; and poly(9,9-dioctylfluorene-*alt*-*N*-(4-*sec*-butylphenyl)-diphenylamine) (TFB) from Sigma-Aldrich.

Perovskite Precursor Solution and Film Deposition: Triple-cation mixed-halide perovskite $(\text{Cs}_{0.06}\text{MA}_{0.15}\text{FA}_{0.79})\text{Pb}(\text{Br}_{0.4}\text{I}_{0.6})_3$ precursor solution was prepared by dissolving PbI_2 (0.65 M), PbBr_2 (0.67 M), formamidinium iodide (1 M), and methylammonium bromide (0.20 M) in a mixture of anhydrous DMF:DMSO (4:1 volume ratio, v:v) followed by addition of 5 vol% from CsI stock solution (1.5 M in DMSO). Glass substrates were cleaned by sonication in acetone and isopropyl alcohol for 30 min, then the substrates were further cleaned with oxygen plasma treatment for 10 min. The perovskite solution was spin-coated on glass substrates in a two-step program at 1000 and 4000 rpm for 10 and 30 s, respectively, and 110 μL of chlorobenzene was poured on the spinning substrate 30 s after the starting of the program. The substrates were then annealed at 100 $^\circ\text{C}$ for 1 h. Synthesis and deposition of perovskite solutions were performed inside a nitrogen glove box under moisture- and oxygen-controlled conditions (H_2O level < 1 ppm; O_2 level < 10 ppm). The thickness of the prepared films was ≈ 550 nm. Films with this thickness were used for all the measurements except the PDS measurement. The samples for the PDS measurement had a thickness of 200 nm and were made from a diluted perovskite solution that was made by addition of 50 vol% from a mixture of anhydrous DMF:DMSO (4:1 volume ratio, v:v) to the main solution. It was noted that all the measurements were performed in ambient laboratory conditions with the humidity range of 40–60%. For making LED device contacts, glass substrates were cleaned and plasma etched with the same method described above. Colloidal AZO nanoparticles were then deposited on the glass substrates in a one-step program at 4000 rpm for 40 s. The perovskite solution was then

spin-coated on the AZO layer using the same spin-coating parameters described above for making perovskite films. Lastly, a solution of TFB in toluene (10 mg mL⁻¹) was spin-coated on top of the perovskite film in a two-step program at 2000 and 5000 rpm for 30 and 10 s, respectively.

Scanning Electron Microscopy: A field-emission scanning electron microscope (FESEM, Merlin) was employed to examine surface morphology of the perovskite film. An electron beam accelerated to 3 kV was used with an in-lens detector.

Photothermal Deflection Spectroscopy: PDS is a scatter-free surface sensitive absorption measurement. Perovskite films were excited with a modulated monochromated light beam perpendicular to the plane of the sample. A combination of a Light Support MKII 100 W xenon arc source and a CVI DK240 monochromator was used to produce a modulated monochromated light beam. The laser probe beam was produced with Qioptiq 670-nm fiber-coupled diode laser and directed parallel to the perovskite film surface. A white-light LED source with an intensity of 100 mW cm⁻² was used to light-soak the perovskite films.

Photoluminescence Characterization: Fluorescence spectra and the external PL quantum efficiency were measured using an integrating sphere and a 532 nm CW laser at an illumination intensity of ≈60 mW cm⁻². A calibrated Andor iDUS DU490A InGaAs detector was used to determine photoluminescence quantum efficiency. The external PLQE was calculated as described elsewhere.^[52]

Time-Resolved Microwave Conductivity: This technique gives a direct measure of the charge-carrier yield, lifetimes, and mobilities by monitoring the photoconductance ΔG upon pulsed laser excitation. The TRMC technique monitors the change in reflected microwave power by the loaded microwave cavity upon pulsed laser excitation. The photoconductance (ΔG) of the samples was deduced from the measured laser-induced change in normalized microwave power. The yield of generated free charges ϕ and mobility $\Sigma\mu = (\mu_e + \mu_h)$ can be obtained by the following equation

$$\phi \Sigma\mu = \frac{\Delta G}{I_0 \beta e F_A} \quad (1)$$

where I_0 is the number of photons per pulse per unit area, β is a geometry constant of the microwave cell, e is the elementary charge, and F_A is the fraction of light absorbed by the film at the incident excitation wavelength.

Grazing-Incidence Wide-Angle X-Ray Scattering: This measurement was taken at beamline I07 of the Diamond Light Source facility. The beam energy was 10 keV and the wavelength was 1.23985 Å. The beam incidence angle was set at 0.3°. The atmosphere-protected measurement chamber was continuously flushed with air or He gas as needed at a rate of 1.5 L min⁻¹. Humid conditions were achieved by bubbling the gas through water before entering the measurement chamber. The recorded level of relative humidity was 50% for the humid air and <5% in dry He conditions. Light soaking of the samples was carried out by placing a 532 nm laser at an intensity of 0.3 suns inside the chamber, shining on the sample. The emitted photoluminescence was collected via an optical fiber coupled to an Ocean Optics Maya2000 Pro spectrometer.

Photoluminescence Microscopy: The PL emission maps were acquired using a wide-field, hyperspectral imaging microscope (Photon etc. IMA VIS), and detected with a front-illuminated, low-noise CCD camera that was thermoelectrically cooled down to 0 °C. A CW, power-tunable 405 nm laser was used as the PL excitation source with an incident photon flux equivalent to 1 sun (spot size diameter ≈ 150 μm). A 420 nm long-pass filter was placed in the detection pathway to block the 405 nm laser reflection. The detection wavelengths were swept from 650 to 850 nm, to ensure full acquisition of the emitted PL spectrum, with a step size = 5 nm and dwell time = 10 s per wavelength. Between PL measurements, the perovskite film was light-soaked with a white-light source at ≈3 suns photon flux (290 mW cm⁻²) at varying time durations. All data were acquired in ambient atmospheric conditions.

Time-Resolved Photoluminescence Measurements: Time-resolved PL spectra were recorded using a gated intensified CCD camera (Andor iStar DH740 CCI-010) connected to a calibrated grating spectrometer (Andor

SR303i). A Ti:sapphire optical amplifier (1 kHz repetition rate, 90 fs pulse width) was used to generate narrow bandwidth photoexcitation (10 nm full-width at half maximum (FWHM)) with a wavelength of 550 nm, via a custom-built noncollinear optical parametric amplifier. Light soaking of perovskite films was performed during the measurement using a laser source with a wavelength of 532 nm and an intensity of 60 mW cm⁻². The emitted steady-state photoluminescence was collected via an optical fiber coupled to an Ocean Optics Maya2000 Pro spectrometer.

Supporting Information

Supporting Information is available from the Wiley Online Library or from the author.

Acknowledgements

Z.A.-G. acknowledges funding from a Winton Studentship, and ICON Studentship from the Lloyd's Register Foundation. S.D.S., M.A., and E.R. acknowledge the European Research Council (ERC) under the European Union's Horizon 2020 research and innovation programme (HYPERION, Grant Agreement No. 756962). S.D.S. thanks the Royal Society and Tata Group (UF150033). The authors thank the Engineering and Physical Sciences Research Council (EPSRC) for support. M.A.-J. thanks Cambridge Materials Limited and EPSRC (Grant No. EP/M005143/1) for their funding and technical support. D.Y.G. acknowledges the funding from the China Scholarship Council (CSC). S.M. acknowledges funding from an EPSRC studentship. A.S., R.S., and R.H.F. acknowledge support from the SUNRISE (EP/P032591/1) project. A.S. and R.H.F. also acknowledge support from UKIERI project, Winton Programme for the Physics of Sustainability (University of Cambridge) and Indo-UK joint project—APEX Phase-II. R.S. acknowledges the Newton–Bhabha international fellowship. S.D.S. and E.M.T. acknowledge funding from the Engineering and Physical Sciences Research Council (EPSRC) under grant reference EP/R023980/1. E.R. was partially supported by an EPSRC Departmental Graduate Studentship. K.G. and S.M. appreciate support from the Polish Ministry of Science and Higher Education within the Mobilnosc Plus program (Grant No.1603/MOB/V/2017/0). K.F. acknowledges a George and Lilian Schiff Studentship, Winton Studentship, the Engineering and Physical Sciences Research Council (EPSRC) studentship, Cambridge Trust Scholarship, and Robert Gardiner Scholarship. This work utilized beamline I07 at the Diamond Light Source (Proposal SI17223-1).

Conflict of Interest

The authors declare no conflict of interest.

Keywords

halide perovskites, luminescence, passivation, photoinduced ion migration, time-resolved spectroscopy

Received: April 13, 2019

Revised: August 15, 2019

Published online:

[1] M. M. Lee, J. Teuscher, T. Miyasaka, T. N. Murakami, H. J. Snaith, *Science* **2012**, 338, 643.

[2] G. Xing, N. Mathews, S. S. Lim, N. Yantara, X. Liu, D. Sabba, M. Grätzel, S. Mhaisalkar, T. C. Sum, *Nat. Mater.* **2014**, 13, 476.

[3] S. D. Stranks, H. J. Snaith, *Nat. Nanotechnol.* **2015**, 10, 391.

- [4] W. S. Yang, J. H. Noh, N. J. Jeon, Y. C. Kim, S. Ryu, J. Seo, S. I. Seok, *Science* **2015**, *348*, 1234.
- [5] N. Wang, L. Cheng, R. Ge, S. Zhang, Y. Miao, W. Zou, C. Yi, Y. Sun, Y. Cao, R. Yang, Y. Wei, Q. Guo, Y. Ke, M. Yu, Y. Jin, Y. Liu, Q. Ding, D. Di, L. Yang, G. Xing, H. Tian, C. Jin, F. Gao, R. H. Friend, J. Wang, W. Huang, *Nat. Photonics* **2016**, *10*, 699.
- [6] S. D. Stranks, G. E. Eperon, G. Grancini, C. Menelaou, M. J. P. Alcocer, T. Leijtens, L. M. Herz, A. Petrozza, H. J. Snaith, *Science* **2013**, *342*, 341.
- [7] H. Oga, A. Saeki, Y. Ogomi, S. Hayase, S. Seki, *J. Am. Chem. Soc.* **2014**, *136*, 13818.
- [8] H. J. Snaith, *J. Phys. Chem. Lett.* **2013**, *4*, 3623.
- [9] S. D. Stranks, *ACS Energy Lett.* **2017**, *2*, 1515.
- [10] F. Deschler, M. Price, S. Pathak, L. E. Klintberg, D. D. Jarausch, R. Higler, S. Hüttner, T. Leijtens, S. D. Stranks, H. J. Snaith, M. Atatüre, R. T. Phillips, R. H. Friend, *J. Phys. Chem. Lett.* **2014**, *5*, 1421.
- [11] S. D. Stranks, V. M. Burlakov, T. Leijtens, J. M. Ball, A. Gorieli, H. J. Snaith, *Phys. Rev. Appl.* **2014**, *2*, 034007.
- [12] D. W. deQuilettes, W. Zhang, V. M. Burlakov, D. J. Graham, T. Leijtens, A. Osherov, V. Bulović, H. J. Snaith, D. S. Ginger, S. D. Stranks, *Nat. Commun.* **2016**, *7*, 11683.
- [13] Y. Yamada, M. Endo, A. Wakamiya, Y. Kanemitsu, *J. Phys. Chem. Lett.* **2015**, *6*, 482.
- [14] D. W. deQuilettes, S. Koch, S. Burke, R. K. Paranjai, A. J. Shropshire, M. E. Ziffer, D. S. Ginger, *ACS Energy Lett.* **2016**, *1*, 438.
- [15] N. K. Noel, A. Abate, S. D. Stranks, E. S. Parrott, V. M. Burlakov, A. Gorieli, H. J. Snaith, *ACS Nano* **2014**, *8*, 9815.
- [16] M. Abdi-Jalebi, Z. Andaji-Garmaroudi, S. Cacovich, C. Stavarakas, B. Philippe, J. M. Richter, M. Alsari, E. P. Booker, E. M. Hutter, A. J. Pearson, S. Lilliu, T. J. Savenije, H. Rensmo, G. Divitini, C. Ducati, R. H. Friend, S. D. Stranks, *Nature* **2018**, *555*, 497.
- [17] J. H. Noh, S. H. Im, J. H. Heo, T. N. Mandal, S. I. Seok, *Nano Lett.* **2013**, *13*, 1764.
- [18] Y. Ogomi, A. Morita, S. Tsukamoto, T. Saitho, N. Fujikawa, Q. Shen, T. Toyoda, K. Yoshino, S. S. Pandey, T. Ma, S. Hayase, *J. Phys. Chem. Lett.* **2014**, *5*, 1004.
- [19] L. Gil-Escrig, A. Miquel-Sempere, M. Sessolo, H. J. Bolink, *J. Phys. Chem. Lett.* **2015**, *6*, 3743.
- [20] G. E. Eperon, T. Leijtens, K. A. Bush, R. Prasanna, T. Green, J. T.-W. Wang, D. P. McMeekin, G. Volonakis, R. L. Milot, R. May, A. Palmstrom, D. J. Slotcavage, R. A. Belisle, J. B. Patel, E. S. Parrott, R. J. Sutton, W. Ma, F. Moghadam, B. Conings, A. Babayigit, H.-G. Boyen, S. Bent, F. Giustino, L. M. Herz, M. B. Johnston, M. D. McGehee, H. J. Snaith, *Science* **2016**, *354*, 861.
- [21] C. M. Sutter-Fella, Y. Li, M. Amani, J. W. Ager, F. M. Toma, E. Yablonovitch, I. D. Sharp, A. Javey, *Nano Lett.* **2016**, *16*, 800.
- [22] K. A. Bush, K. Frohna, R. Prasanna, R. E. Beal, T. Leijtens, S. A. Swifter, M. D. McGehee, *ACS Energy Lett.* **2018**, *3*, 428.
- [23] E. T. Hoke, D. J. Slotcavage, E. R. Dohner, A. R. Bowring, H. I. Karunadasa, M. D. McGehee, *Chem. Sci.* **2015**, *6*, 613.
- [24] S. J. Yoon, S. Draguta, J. S. Manser, O. Sharia, W. F. Schneider, M. Kuno, P. V. Kamat, *ACS Energy Lett.* **2016**, *1*, 290.
- [25] C. G. Bischak, C. L. Hetherington, H. Wu, S. Aloni, D. F. Ogletree, D. T. Limmer, N. S. Ginsberg, *Nano Lett.* **2017**, *17*, 1028.
- [26] A. J. Barker, A. Sadhanala, F. Deschler, M. Gandini, S. P. Senanayak, P. M. Pearce, E. Mosconi, A. J. Pearson, Y. Wu, A. R. Srimath Kandada, T. Leijtens, F. De Angelis, S. E. Dutton, A. Petrozza, R. H. Friend, *ACS Energy Lett.* **2017**, *2*, 1416.
- [27] A. J. Knight, A. D. Wright, J. B. Patel, D. P. McMeekin, H. J. Snaith, M. B. Johnston, L. M. Herz, *ACS Energy Lett.* **2019**, *4*, 75.
- [28] M. C. Brennan, S. Draguta, P. V. Kamat, M. Kuno, *ACS Energy Lett.* **2018**, *3*, 204.
- [29] S. G. Motti, D. Meggiolaro, A. J. Barker, E. Mosconi, C. A. R. Perini, J. M. Ball, M. Gandini, M. Kim, F. De Angelis, A. Petrozza, *Nat. Photonics* **2019**, *13*, 532.
- [30] M. Saliba, T. Matsui, J.-Y. Seo, K. Domanski, J.-P. Correa-Baena, M. K. Nazeeruddin, S. M. Zakeeruddin, W. Tress, A. Abate, A. Hagfeldt, M. Grätzel, *Energy Environ. Sci.* **2016**, *9*, 1989.
- [31] D. P. McMeekin, G. Sadoughi, W. Rehman, G. E. Eperon, M. Saliba, M. T. Hörlantner, A. Haghighirad, N. Sakai, L. Korte, B. Rech, M. B. Johnston, L. M. Herz, H. J. Snaith, *Science* **2016**, *351*, 151.
- [32] N. K. Noel, S. D. Stranks, A. Abate, C. Wehrenfennig, S. Guarnera, A.-A. Haghighirad, A. Sadhanala, G. E. Eperon, S. K. Pathak, M. B. Johnston, A. Petrozza, L. M. Herz, H. J. Snaith, *Energy Environ. Sci.* **2014**, *7*, 3061.
- [33] A. Sadhanala, F. Deschler, T. H. Thomas, S. E. Dutton, K. C. Goedel, F. C. Hanusch, M. L. Lai, U. Steiner, T. Bein, P. Docampo, D. Cahen, R. H. Friend, *J. Phys. Chem. Lett.* **2014**, *5*, 2501.
- [34] D. Di, K. P. Musselman, G. Li, A. Sadhanala, Y. Ievskaya, Q. Song, Z. K. Tan, M. L. Lai, J. L. MacManus-Driscoll, N. C. Greenham, R. H. Friend, *J. Phys. Chem. Lett.* **2015**, *6*, 446.
- [35] A. Sadhanala, A. Kumar, S. Pathak, A. Rao, U. Steiner, N. C. Greenham, H. J. Snaith, R. H. Friend, *Adv. Electron. Mater.* **2015**, *1*, 1500008.
- [36] M. Abdi-Jalebi, M. I. Dar, A. Sadhanala, S. P. Senanayak, M. Franckevičius, N. Arora, Y. Hu, M. K. Nazeeruddin, S. M. Zakeeruddin, M. Grätzel, R. H. Friend, *Adv. Energy Mater.* **2016**, *6*, 1502472.
- [37] R. Brenes, D. Guo, A. Osherov, N. K. Noel, C. Eames, E. M. Hutter, S. K. Pathak, F. Niroui, R. H. Friend, M. S. Islam, H. J. Snaith, V. Bulović, T. J. Savenije, S. D. Stranks, *Joule* **2017**, *1*, 155.
- [38] J. M. Howard, E. M. Tennyson, S. Barik, R. Szostak, E. Waks, M. F. Toney, A. F. Nogueira, B. R. A. Neves, M. S. Leite, *J. Phys. Chem. Lett.* **2018**, *9*, 3463.
- [39] O. G. Reid, M. Yang, N. Kopidakis, K. Zhu, G. Rumbles, *ACS Energy Lett.* **2016**, *1*, 561.
- [40] A. Amat, E. Mosconi, E. Ronca, C. Quarti, P. Umari, M. K. Nazeeruddin, M. Grätzel, F. De Angelis, *Nano Lett.* **2014**, *14*, 3608.
- [41] C. Lin, S. Li, W. Zhang, C. Shao, Z. Yang, *ACS Appl. Energy Mater.* **2018**, *1*, 1374.
- [42] K. W. Tan, D. T. Moore, M. Saliba, H. Sai, L. A. Estroff, T. Hanrath, H. J. Snaith, U. Wiesner, *ACS Nano* **2014**, *8*, 4730.
- [43] S. Colella, E. Mosconi, P. Fedeli, A. Listorti, F. Gazza, F. Orlandi, P. Ferro, T. Besagni, A. Rizzo, G. Calestani, G. Gigli, F. De Angelis, R. Mosca, *Chem. Mater.* **2013**, *25*, 4613.
- [44] A. Osherov, E. M. Hutter, K. Galkowski, R. Brenes, D. K. Maude, R. J. Nicholas, P. Plochocka, V. Bulović, T. J. Savenije, S. D. Stranks, *Adv. Mater.* **2016**, *28*, 10757.
- [45] Y. Tian, M. Peter, E. Unger, M. Abdellah, K. Zheng, T. Pullerits, A. Yartsev, V. Sundström, I. G. Scheblykin, *Phys. Chem. Chem. Phys.* **2015**, *17*, 24978.
- [46] J. F. Galisteo-López, M. Anaya, M. E. Calvo, H. Míguez, *J. Phys. Chem. Lett.* **2015**, *6*, 2200.
- [47] D. W. de Quilettes, S. M. Vorpahl, S. D. Stranks, H. Nagaoka, G. E. Eperon, M. E. Ziffer, H. J. Snaith, D. S. Ginger, *Science* **2015**, *348*, 683.
- [48] D. J. Slotcavage, H. I. Karunadasa, M. D. McGehee, *ACS Energy Lett.* **2016**, *1*, 1199.
- [49] J. M. Richter, M. Abdi-Jalebi, A. Sadhanala, M. Tabachnyk, J. P. H. Rivett, L. M. Pazos-Outón, K. C. Gödel, M. Price, F. Deschler, R. H. Friend, *Nat. Commun.* **2016**, *7*, 13941.
- [50] G. Bongiovanni, J. L. Staehli, *Phys. Rev. B: Condens. Matter. Mater. Phys.* **1992**, *46*, 9861.
- [51] M. Saba, M. Cadelano, D. Marongiu, F. Chen, V. Sarritzu, N. Sestu, C. Figus, M. Aresti, R. Piras, A. Geddo Lehmann, C. Cannas, A. Musinu, F. Quochi, A. Mura, G. Bongiovanni, *Nat. Commun.* **2014**, *5*, 5049.
- [52] J. C. De Mello, H. F. Wittmann, R. H. Friend, *Adv. Mater.* **1997**, *9*, 230.